

Scaling of alloy interfacial properties under compositional strain

Zhi-Feng Huang

Department of Physics and Astronomy, Wayne State University, Detroit, Michigan 48201, USA

(Dated: February 9, 2016)

Complex morphologies and microstructures that emerge during materials growth and solidification are often determined by both equilibrium and kinetic properties of the interface and their crystalline anisotropies. However limited knowledge is available for the alloying and particularly the compositionally generated elastic effects on these interface characteristics. Here we systematically investigate such compositional effects on the interfacial properties of an alloy model system based on the phase-field-crystal analysis, including the solid-liquid interfacial free energy, kinetic coefficient, and lattice pinning strength. Scaling relations for these interfacial quantities over various ranges of material parameters are identified and predicted. Our results indicate the important effects of couplings among mesoscopic and microscopic length scales of alloy structure and concentration, and also the influence of compressive and tensile interface stresses induced by composition variations. The approach developed here provides an efficient way to systematically identify these key material properties beyond the traditional atomistic and continuum methods.

PACS numbers: 81.10.Aj, 68.08.-p, 64.70.dm, 05.70.Np

I. INTRODUCTION

Properties of surfaces and interfaces are among the vital factors controlling material crystallization and microstructural dynamics. Typical examples include the crucial effects of the liquid-solid interfacial free energy on dendritic solidification [1], eutectic or peritectic growth [2, 3], and the evolution of film surface nanostructures such as quantum dots [4] or nanowires [5]. Properties governing system kinetics, in particular the interface mobility or kinetic coefficient (defined as the ratio between interface velocity and undercooling or supersaturation), also significantly affect the material microstructures and morphologies during e.g., crystal nucleation, ordering, and dendrite formation [2, 6, 7].

Despite both fundamental and technological importance of these interfacial properties in the characterization, understanding and modeling of materials growth, it remains a great challenge to experimentally or computationally determine their accurate values, anisotropies, and particularly their variations with material parameters and growth or processing conditions. Significant difficulty exists in the corresponding experimental measurements, with limited data available for the interfacial energy anisotropy of alloys [8, 9] and the interface kinetic coefficient of only few pure metals [10, 11]. Most calculations rely on atomistic simulations via molecular dynamics (MD) and Monte Carlo (MC) methods [2, 6, 12–16], or continuum approaches based on phase field [17], Ginzburg-Landau [18, 19], or classical density functional [20, 21] theory. However, it is computationally challenging to conduct any systematic studies across a reasonable range of material parameters, particularly for alloy systems for which very limited results are available to date. For example, the alloying effect on the kinetic coefficient is not yet understood, with only few data obtained from recent MD simulations of binary ordered phases which estimated the value of kinetic coefficient at the melting

temperature [6, 15, 16]. Most MD and MC studies of alloy solid-liquid interfacial energy have been focused on either zero [13] or a specific finite value [14] of atomic size difference between alloy components, while a systematic understanding of the effects of the associated compositional strain [22, 23], which is known to play an important role on determining material microstructures, properties and growth morphologies, is still lacking.

The focus of this work is on identifying the key factors governing alloy crystal-melt interfacial properties, particularly the effects generated by compositional stresses and by the couplings among mesoscopic structural amplitudes and alloy concentration and the underlying microscopic crystalline lattice. This leads to new scaling behaviors of alloy interfacial free energy γ and kinetic coefficient μ_k , a reversal of γ anisotropy caused by compositional strain, and an interface lattice pinning effect that is crucial in determining system growth mechanisms and dynamics. Our findings reveal that these results not only depend on the interface orientation as expected, but also on the impacts of interface preferential segregation and the corresponding compositionally induced interface stresses.

To obtain a generic understanding of such effects, here we adopt a model alloy system which incorporates the crystalline symmetry from a simple but fundamental aspect. It also enables us to systematically examine the varying conditions of compositional strain. More specifically, we develop a new nonadiabatic complex amplitude approach for binary alloys based on the phase field crystal (PFC) method [24–26]. In PFC models lattice symmetry is built in the system free energy functional via the selection and competition between different modes of characteristic microscopic length scales (e.g., minimum 1 mode for two-dimensional (2D) triangular and three-dimensional (3D) bcc structures [24], 2 modes for fcc and hcp [27, 28], and 3 modes for simple cubic [28] and also some complex 2D phases and superlattices [29]). In this work we focus on the 2D triangular system, to emphasize

the fundamental aspects of the alloying effects and the essential features of our approach which can be readily generalized to other systems. In addition, the properties identified here can be used for the study of various 2D crystallization phenomena such as the epitaxial growth of sub-monolayer islands for metallic alloy overlayers [30] or novel 2D materials [31].

This paper is organized as follows. In Sec. II the complex amplitude formulation for binary alloy system is derived and presented, showing new results of nonadiabatic corrections that originate from the coupling between microscopic and mesoscopic spatial scales. The corresponding interface equations of motion and the analytic expressions of interfacial quantities derived are given in Sec. III. In Sec. IV detailed numerical calculations of liquid-solid interfacial properties are conducted, with new scaling behaviors and effects of compositionally generated stresses being identified and discussed. A brief summary of our results is given in Sec. V.

II. NONADIABATIC AMPLITUDE EQUATIONS FOR BINARY PFC

We start from the PFC model equations governing the dynamics of a dimensionless atomic density variation field $n = (\rho - \rho_l)/\rho_l$ and an alloy concentration field $\psi = (\rho_A - \rho_B)/\rho$ for a binary alloy system, where $\rho = \rho_A + \rho_B$ is the total atomic number density, $\rho_{A(B)}$ is the density of A(B) atoms, and ρ_l is a reference state density. These dynamic equations can be written in a rescaled form [32]

$$\partial n / \partial t = \nabla^2 \frac{\delta F}{\delta n} + m \nabla^2 \frac{\delta F}{\delta \psi} + \nabla \cdot \boldsymbol{\eta}_n, \quad (1)$$

$$\partial \psi / \partial t = m \nabla^2 \frac{\delta F}{\delta n} + \nabla^2 \frac{\delta F}{\delta \psi} + \nabla \cdot \boldsymbol{\eta}_\psi, \quad (2)$$

where the mobility contrast $m = (M_A - M_B)/(M_A + M_B)$ with M_A (M_B) the atomic mobility of alloy component A (B), $\boldsymbol{\eta}_n$ and $\boldsymbol{\eta}_\psi$ are noise fields, and for one-mode PFC the free energy functional is given by

$$F = \int d\mathbf{r} \left\{ -\frac{1}{2} \epsilon n^2 + \frac{1}{2} n (\nabla^2 + q_0^2)^2 n + \frac{1}{3} g_2 n^3 + \frac{1}{4} n^4 + \frac{1}{2} K_0 |\nabla \psi|^2 + \frac{1}{2} (w_0 + 2v_1 n + g n^2) \psi^2 + \frac{1}{4} u_0 \psi^4 + 2\alpha n (\nabla^2 + \nabla^4) (n\psi) \right\}. \quad (3)$$

Here ϵ is proportional to the temperature distance from the melting point, $q_0 = 1$ after rescaling over a length scale of lattice spacing, and g_2 , K_0 , w_0 , v_1 , g , u_0 are phenomenological model parameters determining system properties including elastic moduli and the phase diagram (e.g., eutectic or isomorphous; see Ref. [32] for more detailed description). Also α is the solute expansion coefficient [22] defined as $\alpha = \partial \ln a / \partial \psi$ (with a the alloy lattice constant) which characterizes the atomic size mismatch between alloy components. It gives rise to the

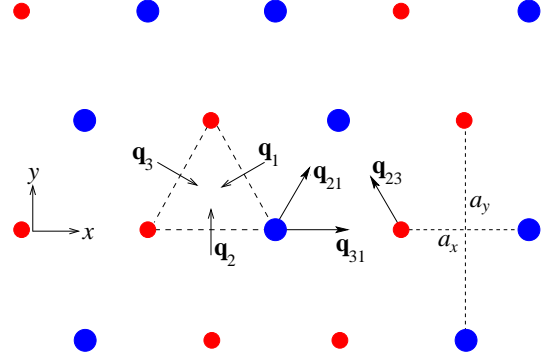


FIG. 1. (Color online) Schematic of a triangular lattice for a binary A-B system. The directions of $\mathbf{q}_j = (1 + \delta_0) \mathbf{q}_j^0$ and $\mathbf{q}_{ij} = \mathbf{q}_i - \mathbf{q}_j$ (with $i, j = 1, 2, 3$) and lattice spacings a_x , $a_y = \sqrt{3}a_x$ are indicated.

compositional strain $\alpha\psi$ generated by local composition variations [22, 23].

In the standard amplitude formulation of a crystalline system [32–34], the density field n is expanded as $n = n_0 + \sum_j A_j e^{i\mathbf{q}_j^0 \cdot \mathbf{r}} + \text{c.c.}$, where n_0 is the average density variation (i.e., $n_0 = (\rho_0 - \rho_l)/\rho_l$ with ρ_0 the average number density) and \mathbf{q}_j^0 are the basic wave vectors of the crystalline lattice ($j = 3$ for triangular structure with $\mathbf{q}_1^0 = -q_0(\sqrt{3}\hat{x}/2 + \hat{y}/2)$, $\mathbf{q}_2^0 = q_0\hat{y}$, and $\mathbf{q}_3^0 = q_0(\sqrt{3}\hat{x}/2 - \hat{y}/2)$). Both the complex amplitudes A_j and alloy concentration field ψ are assumed to vary on “slow” scales that can be separated from the underlying “fast” scales of crystalline lattice. However, for thin enough interfaces such an adiabatic approximation of scale separation is no longer valid, and nonadiabatic corrections [35] are needed to account for the coupling between mesoscopic (amplitudes and concentration) and microscopic (lattice) length scales.

To derive the corresponding nonadiabatic amplitude equations, we follow the procedure of multiple-scale analysis outlined in Refs. [32, 35], including: (i) Separate “slow” vs “fast” scales of $(X = \epsilon^{1/2}x, Y = \epsilon^{1/2}y, T = \epsilon t)$ vs (x, y, t) , and assume concentration field $\psi = \psi(X, Y, T)$, complex amplitudes $A_j = A_j(X, Y, T)$, and $n_0 = n_0(X, Y, T)$ in the expansion of n , (ii) conduct the multiple-scale expansion on the binary PFC equations (1) and (2) and apply the solvability conditions, (iii) keep the nonadiabatic coupling between “slow” and “fast” spatial scales across interfaces of various orientations (e.g., 6 directions for the triangular structure shown in Fig. 1), and (iv) given the bulk compositional elastic effect, rewrite amplitudes $A_j = A'_j e^{i\mathbf{q}_j^0 \cdot \mathbf{u}_c}$ with displacement vector $\mathbf{u}_c = \delta_0 \mathbf{r}$ to address the compositional strain in alloy systems, where $\delta_0 = \sqrt{1 - 2\alpha\psi_s} - 1$ (with ψ_s the equilibrium composition in the solid bulk) can be identified from the corresponding free energy minimization [32]. In the case of triangular symmetry, to the lowest order we obtain

$$\partial A'_1/\partial t = -q_0^2(1-m^2)\frac{\delta\mathcal{F}}{\delta A'_1} - (1-m^2)\int_x^{x\pm a_x}\frac{dx'}{a_x}\int_y^{y+a_y}\frac{dy'}{a_y} \left[f_{p_{11}}e^{i\mathbf{q}_1\cdot\mathbf{r}'} + f_{p_1}e^{-i\mathbf{q}_2\cdot\mathbf{r}'} + f_{p_0}e^{-i\mathbf{q}_3\cdot\mathbf{r}'} + f_{p_{12}}e^{i\mathbf{q}_{12}\cdot\mathbf{r}'} + f_{p_{13}}e^{i\mathbf{q}_{13}\cdot\mathbf{r}'} + f_{p_{33}}^*e^{i\mathbf{q}_{23}\cdot\mathbf{r}'} + f_{p_2}^*e^{i\mathbf{q}_{32}\cdot\mathbf{r}'} \right] + \eta_1, \quad (4)$$

$$\partial A'_2/\partial t = -q_0^2(1-m^2)\frac{\delta\mathcal{F}}{\delta A'_2} - (1-m^2)\int_x^{x\pm a_x}\frac{dx'}{a_x}\int_y^{y+a_y}\frac{dy'}{a_y} \left[f_{p_1}^*e^{-i\mathbf{q}_1\cdot\mathbf{r}'} + f_{p_2}e^{i\mathbf{q}_2\cdot\mathbf{r}'} + f_{p_3}^*e^{-i\mathbf{q}_3\cdot\mathbf{r}'} + f_{p_{21}}e^{i\mathbf{q}_{21}\cdot\mathbf{r}'} + f_{p_{33}}^*e^{i\mathbf{q}_{13}\cdot\mathbf{r}'} + f_{p_{11}}^*e^{i\mathbf{q}_{31}\cdot\mathbf{r}'} + f_{p_{23}}e^{i\mathbf{q}_{23}\cdot\mathbf{r}'} \right] + \eta_2, \quad (5)$$

$$\partial A'_3/\partial t = -q_0^2(1-m^2)\frac{\delta\mathcal{F}}{\delta A'_3} - (1-m^2)\int_x^{x\pm a_x}\frac{dx'}{a_x}\int_y^{y+a_y}\frac{dy'}{a_y} \left[f_{p_0}^*e^{-i\mathbf{q}_1\cdot\mathbf{r}'} + f_{p_3}e^{-i\mathbf{q}_2\cdot\mathbf{r}'} + f_{p_{33}}e^{i\mathbf{q}_3\cdot\mathbf{r}'} + f_{p_{31}}e^{i\mathbf{q}_{31}\cdot\mathbf{r}'} + f_{p_2}^*e^{i\mathbf{q}_{12}\cdot\mathbf{r}'} + f_{p_{11}}^*e^{i\mathbf{q}_{21}\cdot\mathbf{r}'} + f_{p_{32}}e^{i\mathbf{q}_{32}\cdot\mathbf{r}'} \right] + \eta_3, \quad (6)$$

$$\partial n_0/\partial t = \nabla^2\frac{\delta F}{\delta n_0} + m\nabla^2\frac{\delta\mathcal{F}}{\delta\psi} - \int_x^{x\pm a_x}\frac{dx'}{a_x}\int_y^{y+a_y}\frac{dy'}{a_y} \left[(f_{p_0} + mf_{p'_0})e^{i\mathbf{q}_{13}\cdot\mathbf{r}'} + (f_{p_1} + mf_{p'_1})e^{i\mathbf{q}_{12}\cdot\mathbf{r}'} + (f_{p_3} + mf_{p'_3})e^{i\mathbf{q}_{32}\cdot\mathbf{r}'} + \text{c.c.} \right] + \nabla \cdot \boldsymbol{\eta}_0, \quad (7)$$

$$\partial\psi/\partial t = m\nabla^2\frac{\delta F}{\delta n_0} + \nabla^2\frac{\delta\mathcal{F}}{\delta\psi} - \int_x^{x\pm a_x}\frac{dx'}{a_x}\int_y^{y+a_y}\frac{dy'}{a_y} \left[(mf_{p_0} + f_{p'_0})e^{i\mathbf{q}_{13}\cdot\mathbf{r}'} + (mf_{p_1} + f_{p'_1})e^{i\mathbf{q}_{12}\cdot\mathbf{r}'} + (mf_{p_3} + f_{p'_3})e^{i\mathbf{q}_{32}\cdot\mathbf{r}'} + \text{c.c.} \right] + \nabla \cdot \boldsymbol{\eta}_{\psi_0}, \quad (8)$$

where $a_x = 2\pi/q_x$ and $a_y = 4\pi/q_y$ are lattice spacings, $q_y = q_0(1 + \delta_0)$, $q_x = \sqrt{3}q_y/2$, $\mathbf{q}_j = (1 + \delta_0)\mathbf{q}_j^0$, $\mathbf{q}_{ij} = \mathbf{q}_i - \mathbf{q}_j$, and the integration terms are the nonadiabatic corrections representing the coupling between “slow” and “fast” length scales (i.e., meso-micro scale coupling) which is missing in previous amplitude analysis of alloy systems [32, 34]. Coefficients $f_{p_{ij}}$, f_{p_j} and $f_{p'_j}$ are functions of slowly-varying amplitudes A'_j , n_0 , and concentration field ψ , i.e.,

$$\begin{aligned} f_{p_0} &= 3q_0^2 \left[(6n_0 + 2g_2)A'_1A'_3 + 3 \left(A_1'^2A'_2 + A_2'^*A_3'^* \right) \right], \\ f_{p_1} &= 3q_0^2 \left[(6n_0 + 2g_2)A'_1A'_2 + 3 \left(A_1'^2A'_3 + A_2'^*A_3'^* \right) \right], \\ f_{p_2} &= 4q_0^2 \left[(3n_0 + g_2)A_2'^2 + 6A_1'^*A'_2A'_3 \right], \\ f_{p_3} &= 3q_0^2 \left[(6n_0 + 2g_2)A_2'^*A'_3 + 3 \left(A_1'A_3'^2 + A_1'^*A_2'^* \right) \right], \\ f_{p_{11}} &= 4q_0^2 \left[(3n_0 + g_2)A_1'^2 + 6A_1'A_2'^*A_3'^* \right], \\ f_{p_{33}} &= 4q_0^2 \left[(3n_0 + g_2)A_3'^2 + 6A_1'^*A_2'^*A_3' \right], \\ f_{p_{jk}} &= 21q_0^2A_j'^2A_k'^* \quad (j \neq k), \\ f_{p'_0} &= 6q_0^2 \left[f_\psi A'_1A'_3 - q_0^2\alpha \left(A'_1\mathcal{G}_3'^*A_3'^* + A_3'^*\mathcal{G}_1'A_1' \right) \right], \\ f_{p'_1} &= 6q_0^2 \left[f_\psi A'_1A'_2 - q_0^2\alpha \left(A'_1\mathcal{G}_2'^*A_2'^* + A_2'^*\mathcal{G}_1'A_1' \right) \right], \\ f_{p'_3} &= 6q_0^2 \left[f_\psi A'_3A_2'^* - q_0^2\alpha \left(A'_3\mathcal{G}_2'^*A_2'^* + A_2'^*\mathcal{G}_3'A_3' \right) \right], \end{aligned} \quad (9)$$

where

$$\begin{aligned} f_\psi &= g\psi + 2q_0^2\delta_1^0\alpha, \quad \delta_1^0 = -2q_0^2\alpha\psi_s, \quad (10) \\ \mathcal{G}'_{1,3} &= \nabla^2 \mp 2iq_x\partial_x - iq_y\partial_y, \quad \mathcal{G}'_2 = \nabla^2 + 2iq_y\partial_y. \end{aligned} \quad (11)$$

In the above amplitude equations the noise terms satisfy the conditions (with $i, j = 1, 2, 3$, $\mu, \nu = x, y$, $\vartheta_i = \vartheta_0 = \vartheta_\psi = \vartheta = 1/7$, T the temperature, and Γ a rescaled

constant [32])

$$\begin{aligned} \langle \eta_j \rangle &= \langle \boldsymbol{\eta}_0 \rangle = \langle \boldsymbol{\eta}_{\psi_0} \rangle = 0, \\ \langle \eta_i \eta_j \rangle &= \langle \boldsymbol{\eta}_0 \eta_j \rangle = \langle \boldsymbol{\eta}_0 \eta_j^* \rangle = \langle \boldsymbol{\eta}_{\psi_0} \eta_j \rangle = \langle \boldsymbol{\eta}_{\psi_0} \eta_j^* \rangle = 0, \\ \langle \eta_i \eta_j^* \rangle &= 2(1-m^2)\vartheta_i q_0^2 \Gamma k_B T \delta(\mathbf{r} - \mathbf{r}') \delta(t - t') \delta_{ij}, \\ \langle \eta_0^\mu \eta_0^\nu \rangle &= 2\vartheta_0 \Gamma k_B T \delta(\mathbf{r} - \mathbf{r}') \delta(t - t') \delta^{\mu\nu}, \\ \langle \eta_{\psi_0}^\mu \eta_{\psi_0}^\nu \rangle &= 2\vartheta_\psi \Gamma k_B T \delta(\mathbf{r} - \mathbf{r}') \delta(t - t') \delta^{\mu\nu}, \\ \langle \eta_{\psi_0}^\mu \eta_0^\nu \rangle &= 2m\vartheta_\psi \Gamma k_B T \delta(\mathbf{r} - \mathbf{r}') \delta(t - t') \delta^{\mu\nu}. \end{aligned} \quad (12)$$

In Eqs. (4)–(8) the free energy functional \mathcal{F} is given by

$$\mathcal{F} = \int d\mathbf{r} \left[\sum_j |\mathcal{G}'_j A'_j|^2 + \frac{1}{2} K_0 |\nabla\psi|^2 - \sum_j (2q_0^2\alpha\psi + \delta_1^0) (A'_j \mathcal{G}'_j A'_j + \text{c.c.}) + f(A'_j, n_0, \psi) \right], \quad (13)$$

where f is the bulk free energy density, i.e.,

$$\begin{aligned} f &= \sum_j \left(-\epsilon + 3n_0^2 + 2g_2n_0 + \delta_1^{02} + 4q_0^2\delta_1^0\alpha\psi \right) |A'_j|^2 \\ &+ \frac{3}{2} \sum_j |A'_j|^4 + (6n_0 + 2g_2) \left(\prod_j A'_j + \text{c.c.} \right) \\ &+ 6 \sum_{j < k} |A'_j|^2 |A'_k|^2 + \frac{1}{2} (-\epsilon + q_0^4) n_0^2 + \frac{1}{3} g_2 n_0^3 + \frac{1}{4} n_0^4 \\ &+ \left(\frac{1}{2} w_0 + \frac{1}{2} g n_0^2 + v_1 n_0 + g \sum_j |A'_j|^2 \right) \psi^2 + \frac{1}{4} u_0 \psi^4. \end{aligned} \quad (14)$$

Note that the free energy functional given in Eq. (13) (and also Eq. (3)) is invariant with respect to $\alpha \rightarrow -\alpha$ and $\psi \rightarrow -\psi$. Also the free energy terms in Eqs. (13)

and (14) incorporate the coupling between composition profile and system elasticity and also between mesoscopic structural amplitudes and alloy concentration (i.e., meso-meso scale coupling).

To identify the elastic energy of this alloy system, we

$$F_{\text{elastic}} = \int d\mathbf{r} \left\{ 3q_0^4 (1 + \delta_0^2) \phi^2 \left[\frac{3}{2} (u_{xx}^2 + u_{yy}^2) + u_{xx}u_{yy} + 2u_{xy}^2 \right] + 3\delta_1^0 (4q_0^2 \alpha \psi + \delta_1^0) \phi^2 \right. \\ \left. - 12 (q_0^2 \alpha \psi + \delta_1^0) \phi \nabla^2 \phi + 3q_0^2 (2q_0^2 \alpha \psi + \delta_1^0) \phi^2 [2(1 + \delta_0) (u_{xx} + u_{yy}) + u_{xx}^2 + u_{yy}^2 + 2(u_{xy}^2 + \Omega_{xy}^2)] \right\} \quad (15)$$

where $u_{ij} = (\partial_i u_j^s + \partial_j u_i^s)/2$ is the linear strain tensor and $\Omega_{ij} = (\partial_i u_j^s - \partial_j u_i^s)/2$ is the rotation tensor [22]. Terms in the 2nd line of Eq. (15) incorporate the compositionally-induced interface elastic effects, given that both $\phi \nabla^2 \phi$ and $2q_0^2 \alpha \psi + \delta_1^0 = 2q_0^2 \alpha (\psi - \psi_s)$ are nonzero only around the interface. These terms drive the process of solute preferential segregation towards the liquid-solid interface and determine whether the local elastic deformation is compressive or tensile (noting that around the interface $\psi - \psi_s > 0$ for $\psi_s < 0$ but $\psi - \psi_s < 0$ for $\psi_s > 0$), as will be further discussed in Sec. IV.

III. INTERFACE EQUATIONS OF MOTION WITH SCALE COUPLING AND PINNING EFFECTS

The above nonadiabatic amplitude equations can be further coarse-grained to derive the interface equations of motion. We first apply the projection operator method [36] around a fixed interface orientation $\theta = \theta_0$ (the angle between the interface normal $\hat{\mathbf{n}}$ and the vertical $\hat{\mathbf{y}}$ direction), so that different scales of variations can be separated for local curvilinear coordinates u (along $\hat{\mathbf{n}}$) and s . The results are then extended to the general case of θ via a variation scheme [37, 38] for the system free energy. Detailed procedure and the resulting interface equations are given in Appendix A. Here we focus on a simplified case for which n_0 is assumed to be a constant due to the secondary effect of its variation in an alloy system. At the liquid-solid interface the anisotropic form of the generalized Gibbs-Thomson relation is then given by

$$\mu_k^{-1}(\theta, m)v_n = -\Delta - (\gamma + \gamma'')\kappa - p_0(\theta) \sin(qh_n + \varphi) + \eta_v, \quad (16)$$

where v_n is the normal velocity of the interface, κ is the local curvature, h_n represents the interface height, $q = |\mathbf{q}_j|$ or $|\mathbf{q}_{ij}|$, and η_v is a noise term. The interface supersaturation is given by $\Delta = q_0^2 \Delta \psi_0 \delta \mu_\psi(u = 0, s)$ (the same expression as that of Ref. [39] for isothermal solidification), where the miscibility gap $\Delta \psi_0 = \psi_0(+\infty) - \psi_0(-\infty) \equiv \psi_l - \psi_s$, the chemical potential $\mu_\psi(u, s) = \delta \mathcal{F} / \delta \psi$, and $\delta \mu_\psi = \mu_\psi - \mu_\psi^{\text{eq}}$ with μ_ψ^{eq} the equilibrium value determined by one-dimensional (1D)

rewrite the amplitudes as $A'_j = |A_j| e^{i\mathbf{q}_j^0 \cdot \mathbf{u}_s} \equiv \phi e^{i\mathbf{q}_j^0 \cdot \mathbf{u}_s}$ in the limit of small deformations, where $\mathbf{u}_s = (u_x^s, u_y^s)$ is the displacement field and $\phi = |A_j|$. Substituting it into Eq. (13) we obtain the system elastic energy (to the leading order)

solutions $\psi_0(u)$ and $A_j^0(u)$ governing liquid-solid coexistence (see Eqs. (A1)–(A3) in Appendix A). The interface at $u = 0$ is defined as a Gibbs surface satisfying the condition $\int_{-\infty}^{+\infty} du [\psi_0(u) - \psi_0(\pm\infty)] = 0$. In Eq. (16) the interfacial free energy is expressed as

$$\gamma(\theta) = q_0^2 \int_{-\infty}^{+\infty} du \left\{ K_0 (\partial_u \psi_0)^2 + 4 \sum_j [|\partial_u^2 A_j^0|^2 + (\beta_j^2/2 + 2q_0^2 \alpha \psi_0 + \delta_1^0) |\partial_u A_j^0|^2 + q_0^2 \alpha (\partial_u |A_j^0|^2) (\partial_u \psi_0)] \right. \\ \left. + 2 \sum_j (\partial_\theta \beta_j) [i(\partial_u^2 A_j^0) (\partial_u A_j^{0*}) + \text{c.c.}] \right\}, \quad (17)$$

with $\beta_{1,3} = \mp 2q_x \cos \theta + q_y \sin \theta = 2q_y \sin(\theta \mp \pi/3)$ and $\beta_2 = -2q_y \sin \theta$, and the kinetic coefficient $\mu_k(\theta, m)$ is determined by

$$\mu_k^{-1} = \int \frac{du}{1 - m^2} \left\{ 2 \sum_j |\partial_u A_j^0|^2 + q_0^2 [\psi_0^2 - \psi_0^2(\pm\infty)] \right\}. \quad (18)$$

An important feature incorporated in Eq. (16) is the coupling to the underlying lattice structure, which results in a sine-Gordon type term $p_0 \sin(qh_n + \varphi)$ resembling a periodic pinning potential. The corresponding lattice pinning strength p_0 and phase φ are orientation-dependent, i.e.,

$$p_0 e^{i\varphi} = 2i [p_A(\theta) + p_\psi(\theta)], \quad (19)$$

where p_A originates from the meso-micro scaling coupling for amplitudes A'_j given in Eqs. (4)–(6), while p_ψ originates from the scale coupling of ψ field in Eq. (8), with $p_\psi = 0$ at $\theta = 0, \pm\pi/3$ (\mathbf{q}_j directions) and $p_\psi \neq 0$ at $\theta = \pi/2, \pm\pi/6$ (\mathbf{q}_{ij} orientations). Specifically,

$$p_\psi = q_0^2 \left\{ \left[\int_0^{+\infty} du \psi_0(u) \int_u^{+\infty} du' - \int_{-\infty}^0 du \psi_0(u) \int_{-\infty}^u du' \right] I(u') - \left(\int_0^{+\infty} du [\psi_0 - \psi_0(+\infty)] \right) \int_{-\infty}^{+\infty} du I(u) \right\}, \quad (20)$$

where $I(u) = \int_u^{u+a_x} du' e^{iqu'} f_{p'_k}^*(u')/a_x$ with $k = 0, 1, 3$ for orientations $\theta = \pi/2$ (for \mathbf{q}_{31}), $\pi/6$ (for \mathbf{q}_{21}), and $-\pi/6$ (for \mathbf{q}_{23}) respectively. Also,

$$p_A(\theta = 0) = \int_{-\infty}^{+\infty} du e^{iqu} (A_1^0 \partial_u f_{p_1}^* + A_2^{*0} \partial_u f_{p_2} + A_3^0 \partial_u f_{p_3}^*), \quad (q = q_y, \text{ for direction } \mathbf{q}_2) \quad (21)$$

$$p_A(\theta = \pi/3) = \int_{-\infty}^{+\infty} du e^{iqu} (A_1^0 \partial_u f_{p_{11}}^* + A_2^{*0} \partial_u f_{p_1}^* + A_3^{*0} \partial_u f_{p_0}^*), \quad (q = q_y, \text{ for direction } -\mathbf{q}_1) \quad (22)$$

$$p_A(\theta = -\pi/3) = \int_{-\infty}^{+\infty} du e^{iqu} (A_1^{*0} \partial_u f_{p_0} + A_2^{*0} \partial_u f_{p_3}^* + A_3^0 \partial_u f_{p_{33}}^*), \quad (q = q_y, \text{ for direction } -\mathbf{q}_3) \quad (23)$$

$$p_A(\theta = \pi/2) = \int_{-\infty}^{+\infty} du e^{iqu} (A_1^0 \partial_u f_{p_{13}}^* + A_2^0 \partial_u f_{p_{33}} + A_2^{*0} \partial_u f_{p_{11}}^* + A_3^{*0} \partial_u f_{p_{31}}), \quad (q = 2q_x, \text{ for direction } \mathbf{q}_{31}) \quad (24)$$

$$p_A(\theta = \pi/6) = \int_{-\infty}^{+\infty} du e^{iqu} (A_1^0 \partial_u f_{p_{12}}^* + A_2^{*0} \partial_u f_{p_{21}} + A_3^0 \partial_u f_{p_2} + A_3^{*0} \partial_u f_{p_{11}}^*), \quad (q = 2q_x, \text{ for direction } \mathbf{q}_{21}) \quad (25)$$

$$p_A(\theta = -\pi/6) = \int_{-\infty}^{+\infty} du e^{iqu} (A_1^0 \partial_u f_{p_2} + A_1^{*0} \partial_u f_{p_{33}}^* + A_2^{*0} \partial_u f_{p_{23}} + A_3^0 \partial_u f_{p_{32}}^*), \quad (q = 2q_x, \text{ for direction } \mathbf{q}_{23}) \quad (26)$$

Given the condition $q_x = \sqrt{3}q_y/2$, from Eqs. (17)–(26) and also Eqs. (A1)–(A5) it can be shown that these interfacial quantities γ , μ_k , and p_0 are periodic functions of orientation angle θ with a periodicity of $\pi/3$, consistent with the triangular symmetry of the system. Thus results for directions \mathbf{q}_2 and $-\mathbf{q}_{1,3}$ (with $\theta = 0, \pm\pi/3$) are equivalent; so are the results for directions \mathbf{q}_{31} , \mathbf{q}_{21} and \mathbf{q}_{23} (with $\theta = \pi/2, \pm\pi/6$).

In addition, the continuity condition at the solid-liquid interface (i.e., $u = 0$) is given by

$$v_n \Delta \psi_0 = (1 - m^2) \left[(\nabla \delta \mu_\psi)_{\text{solid}} - (\nabla \delta \mu_\psi)_{\text{liquid}} \right] \cdot \hat{\mathbf{n}}. \quad (27)$$

Here $\delta \mu_\psi(u, s)$ is determined by the solutions of variations $\delta A_j = A_j' - A_j^0(\pm\infty)$ and $\delta \psi = \psi - \psi_0(\pm\infty)$ that are governed by

$$\left. \frac{\partial f}{\partial A_j^*} \right|_1 = 0, \quad \frac{\partial \delta \psi}{\partial t} = (1 - m^2) \nabla^2 \delta \mu_\psi = (1 - m^2) \nabla^2 \left. \frac{\partial f}{\partial \psi} \right|_1, \quad (28)$$

where “ $|_1$ ” refers to the expansion of $\partial f / \partial A_j^*$ or $\partial f / \partial \psi$ to 1st order of δA_j and $\delta \psi$.

Note that three key features have been intrinsically incorporated in the above formulation of interfacial properties: i) meso-meso and meso-micro scale couplings, ii) crystalline anisotropy, and importantly, iii) compositionally generated elastic effects. These will be further illustrated in the numerical results summarized in the next section.

IV. PROPERTIES OF ALLOY SOLID-LIQUID INTERFACE

The analytic results given in Eqs. (17)–(26) allow us to accurately and systematically determine the crystal-melt interfacial properties for binary alloys. Here we focus on a sample eutectic system, with model parameters $(n_0, w_0, g, g_2, u_0, K_0, v_1) = (-0.2, 0.1, -1.8, -0.6, 4, 1, 0)$, and numerically calculate the interfacial free energy γ , kinetic coefficient μ_k , and lattice pinning strength p_0 over various ranges of parameters α (the solute expansion coefficient) and ϵ (the effective reduced temperature) at different interface orientations θ . The corresponding eutectic phase diagrams can be constructed analytically based on the free energy density determined by Eq. (14), with

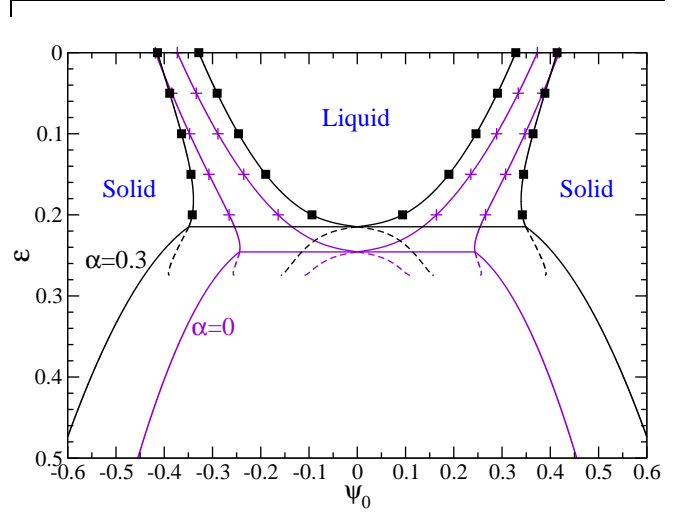


FIG. 2. (Color online) Eutectic phase diagrams obtained from the complex amplitude model with 2D triangular symmetry, for $\alpha = 0$ and 0.3 , and $(n_0, w_0, g, g_2, u_0, K_0, v_1) = (-0.2, 0.1, -1.8, -0.6, 4, 1, 0)$. Dashed lines are metastable extensions of the liquidus and solidus curves. The symbols indicate some of the data points used in our calculations of solid-liquid interfacial properties. Phase diagrams for other values of α and the corresponding data points used are similar.

some sample results shown in Fig. 2. Although in these phase diagrams the $\psi_{s(l)}$ values for positive and negative branches of solidus (liquidus) lines are symmetric, the associated interfacial properties (i.e., γ , μ_k , and p_0) are different due to the effect of compositional strain at the interface. The corresponding numerical results are given below in Figs. 3–14.

A. Interfacial free energy

We have calculated the interfacial free energy γ from Eq. (17) for various interface orientations, with θ values ranging from 0 to $\pi/3$ that are determined from directions of $k\mathbf{q}_i - l\mathbf{q}_j$ (with $i, j = 1, 2, 3$ and k, l integers). Our results shown in Fig. 3 indicate that γ increases with decreasing (or increasing) system temperature (or ϵ value) and increasing miscibility gap $\Delta\psi_0$, for all different values of α and ϵ parameters. This is consistent with experimental measurements of e.g., Zn-Sn, Zn-In, and Al-Sn eutectic systems [40] and also the phase field modeling

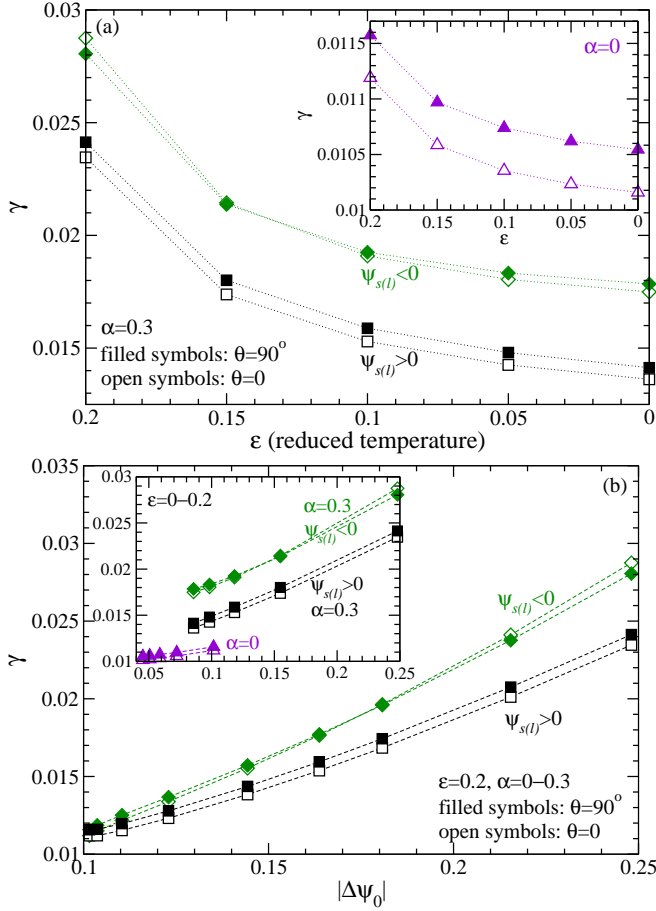


FIG. 3. (Color online) (a) The solid-liquid interfacial free energy γ as a function of reduced temperature ϵ , for $\alpha = 0.3$ and $\alpha = 0$ (inset). (b) γ as a function of miscibility gap $\Delta\psi_0$. Filled or open symbols correspond to the \hat{x} ($\theta = \pi/2$) or \hat{y} ($\theta = 0$) interface orientation. Results for both positive and negative solidus (liquidus) alloy compositions $\psi_{s(l)}$ are shown.

of Ni-Cu isomorphous alloy [17]. This can be attributed to the larger composition gradient $\partial_u \psi_0^0$ around the interface for larger $\Delta\psi_0$. It leads to the increase of compositional free energy (see Eq. (13)) which is absent in the excess configurational entropy theory for single-component systems [41]. Interestingly, at a given interface orientation results of γ for different ranges of ϵ and α fall onto a scaling relation as a function of Young's modulus E , as illustrated in Fig. 4. Parameters of this scaling curve depend on the selection of either positive ($\psi_{s(l)} > 0$) or negative ($\psi_{s(l)} < 0$) branch of solidus-liquidus lines due to different effect of compositional strain caused by nonzero α (see below for more discussions). Actually similar type of data collapse vs E has been obtained from measurement data of surface free energy for some pure metals and alloys (although with different scaling relation for those solid-vapor results) [42], yielding the correlation between solid surface energy and mechanical property of materials.

For triangular symmetry the anisotropy of interfacial

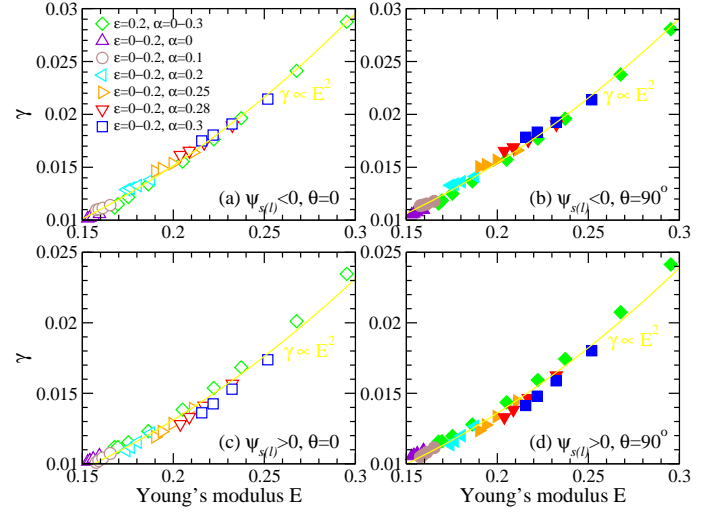


FIG. 4. (Color online) Scaling of γ as a function of Young's modulus E .

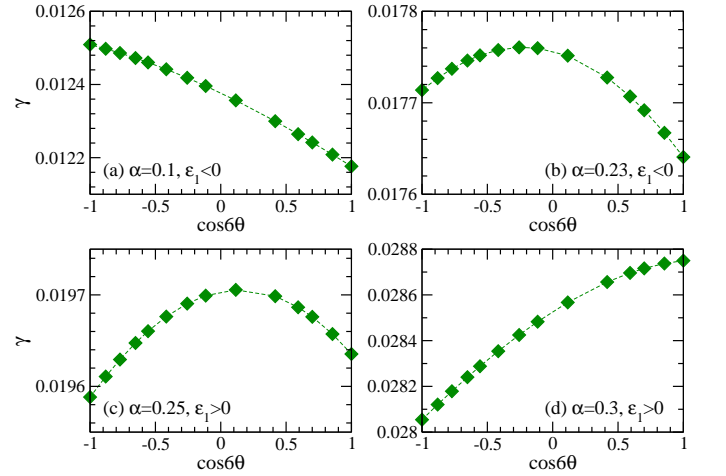


FIG. 5. (Color online) Sample plots of interfacial free energy γ vs $\cos 6\theta$, for $\psi_{s(l)} < 0, \epsilon = 0.2$, and $\alpha = 0.1, 0.23, 0.25, 0.3$.

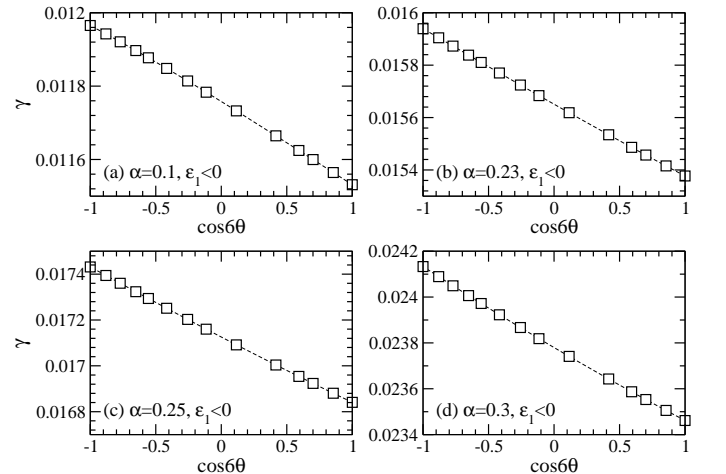


FIG. 6. Sample plots of interfacial free energy γ vs $\cos 6\theta$, for $\psi_{s(l)} > 0, \epsilon = 0.2$, and $\alpha = 0.1, 0.23, 0.25, 0.3$.

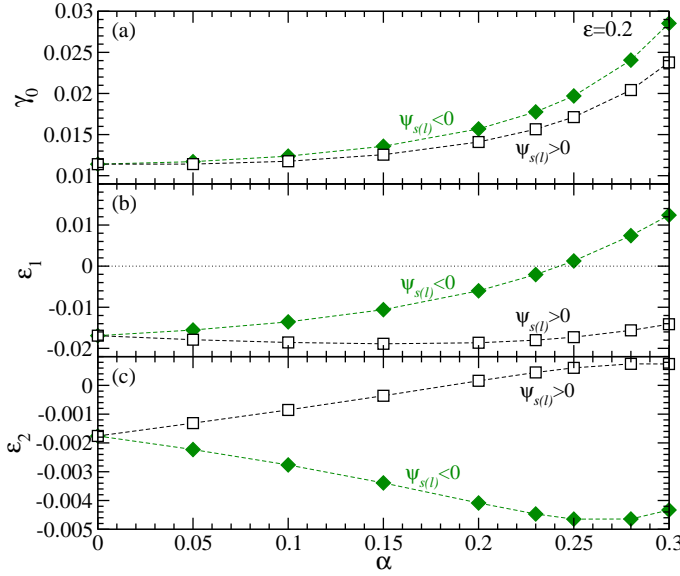


FIG. 7. (Color online) γ_0 and anisotropy parameters ε_1 , ε_2 vs α at $\varepsilon = 0.2$.

energy can be represented by the expansion

$$\gamma = \gamma_0(1 + \varepsilon_1 \cos 6\theta + \varepsilon_2 \cos^2 6\theta + \dots), \quad (29)$$

where ε_1 and ε_2 are anisotropic parameters. In previous studies usually only the 1st-order expansion (ε_1) is kept. The approach given in Eq. (17) can accurately determine even very weak anisotropy of γ , and our numerical data can be well fitted into this 2nd-order form, as shown in Figs. 5 and 6 for negative ($\psi_{s(l)} < 0$) and positive ($\psi_{s(l)} > 0$) solidus/liquidus branches respectively. The corresponding results for parameters γ_0 , ε_1 and ε_2 are given in Fig. 7. Note that for $\psi_{s(l)} > 0$ ε_2 is around an order of magnitude smaller than ε_1 , but they can be of similar order for large enough α when $\psi_{s(l)} < 0$. Also γ_0 increases with the magnitude of α due to larger contribution of compositional strain.

The important role played by the alloy compositional strain is further illustrated by its effect on the anisotropic parameter ε_1 (Fig. 7(b)): For $\psi_{s(l)} < 0$ the increase of α leads to a reversal of sign of ε_1 (see also Fig. 5), and thus a shape change (with a rotation of 30°) in the polar plots of γ and interfacial stiffness $\gamma + \gamma''$ given in Fig. 8(a); however no such changes occur for $\psi_{s(l)} > 0$ (see Figs. 6, 7(b), and 8(b)), which instead gives a weak dependence of ε_1 on α . This difference indicates an asymmetric effect of compressive vs tensile compositional stress at the interface. For $\alpha > 0$ (corresponding to larger size of atom A compared to atom B), $\psi_{s(l)} < 0$ indicates the abundance of smaller-size B atoms in the alloy. In the solid surface layer where $\psi > \psi_s$ (given $\psi_s < \psi_l < 0$), a surface enrichment of larger atoms A occurs, resulting in a compressive solid surface layer with respect to the bulk, and its contribution to the excess interface free energy increases with α (see the interface elastic energy terms given in Eq. (15)). When the anisotropy of this interface

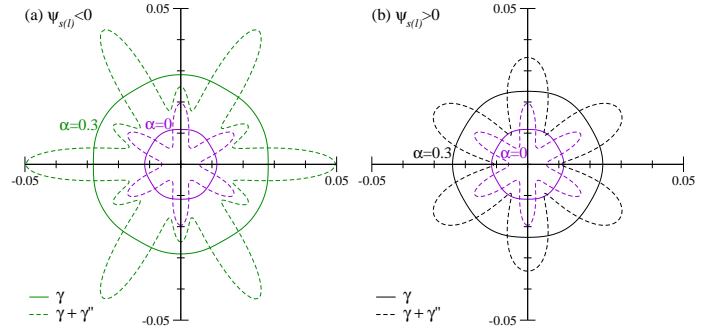


FIG. 8. (Color online) Polar plots of interfacial free energy γ (solid lines) and stiffness $\gamma + \gamma''$ (dashed) for $\varepsilon = 0.2$, $\alpha = 0$ and 0.3 .

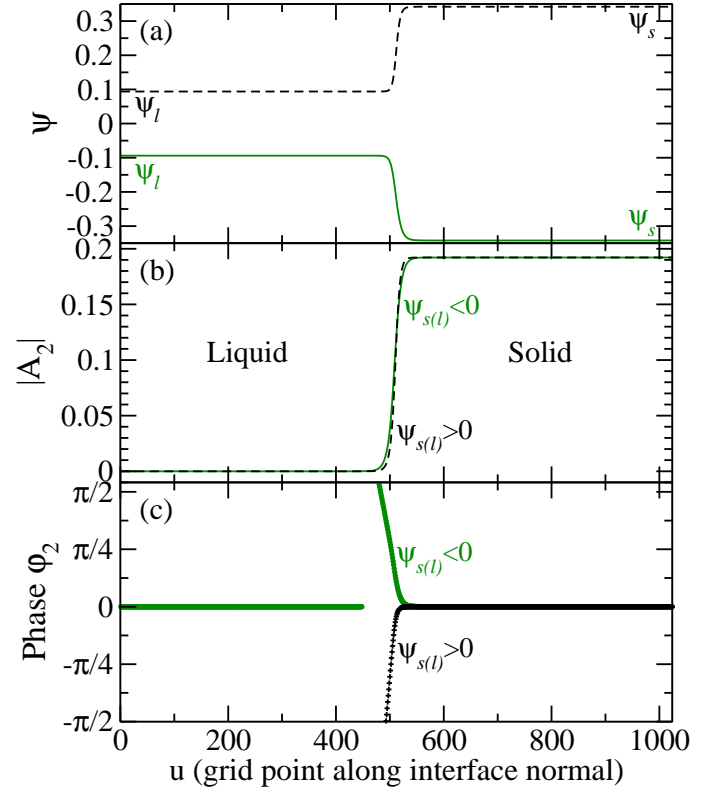


FIG. 9. (Color online) Solid-liquid coexistent profiles of (a) ψ , (b) $|A_2|$, and (c) phase φ_2 , for both positive and negative solidus/liquidus branches with $\varepsilon = 0.2$, $\alpha = 0.3$, $\theta = 0$, and $(n_0, w_0, g, g_2, u_0, K_0, v_1) = (-0.2, 0.1, -1.8, -0.6, 4, 1, 0)$.

elastic energy contribution is opposite to that of the non-compositional ones, the sign of ε_1 would then reverse at large enough α as seen in Fig. 7(b). On the other hand, our results of ε_1 for $\psi_{s(l)} > 0$ indicate that such anisotropy contrast does not exist (or is too weak) for the tensile-stress interface characterized by the enrichment of smaller B atoms (at least for the range of α values examined in our numerical calculations).

To verify this compositionally-induced interface stress, as in Sec. II we rewrite $A'_j = |A_j| \exp(i\mathbf{q}_j^0 \cdot \mathbf{u}_s)$, where

$\mathbf{q}_j^0 \cdot \mathbf{u}_s \equiv \varphi_j$ is the phase of the complex amplitude. Its gradient along the interface normal, $\partial_u \varphi_j$, will then yield the local strain of the system. In the equilibrium state this gradient always vanishes in the bulk and would be nonzero around the solid-liquid interface if the above scenario of surface preferential segregation occurs. This has indeed been seen in our numerical results of A_j^0 , as obtained from solving the 1D amplitude equations (A1)–(A3) at various interface orientations θ . A sample result is presented in Fig. 9, showing equilibrium interfacial profiles of amplitude and concentration for both $\psi_{s(l)} > 0$ and $\psi_{s(l)} < 0$ of solid-liquid coexistence. As shown in Fig. 9(c), the phase $\varphi_j = 0$ in the solid bulk and is nonzero only around the interface, yielding opposite sign of gradient $\partial_u \varphi_j$ for positive vs negative $\psi_{s(l)}$ when $\alpha \neq 0$. This gives rise to different type of interface strain, i.e., tensile vs compressive, which is attributed to the phenomenon of interface segregation and deformation as discussed above. Similar results can be found in our calculations with other choices of parameters (e.g., ϵ , θ , and nonzero α). Note that the surface/interface stress identified here is different from the single-component case, for which nonzero phase φ_j and its spatial gradient around the interface have also been obtained in our solutions of amplitude equations. However, in the alloy system studied here we have additional surface/interface stress generated by compositional effect, giving opposite type of strain for positive vs negative solidus/liquidus branch which is absent in the single-component system and only occurs when $\alpha \neq 0$.

B. Interface kinetic coefficient

For the kinetic coefficient μ_k , to the best of our knowledge results for eutectic or isomorphous systems are still lacking, either from experiments or atomistic simulations, while only limited MD data is available for B2 and B33 ordered phases at the melting temperature (Cu₅₀Zr₅₀ B2, Ni₅₀Al₅₀ B2 and Ni₅₀Zr₅₀ B33 [6, 15, 16]). For the eutectic system examined here, our calculations indicate a change of sign of μ_k from positive to negative at large enough miscibility gap (with large enough ϵ , i.e., not close to the melting point, or large α). This can be seen in Fig. 10, which also shows the decrease of inverse kinetic coefficient μ_k^{-1} with the increase of ϵ and α . This is consistent with the previous phase field study [36] which showed that for a growing interface with $\mu_k < 0$, the relaxation of the interface profile would lag behind the advancing front. Note that these results are obtained under isothermal condition, with the thermodynamic driving force Δ being the interface supersaturation of alloy concentration. It is different from many previous studies of single-component systems based on interface undercooling, although the basic mechanisms inside are similar [39].

Weak crystalline anisotropy of μ_k and its dependence on the compositional strain (or α) are found in our calculations for this alloy system of triangular structure. For the sample results given in Fig. 11, around 2% – 8%

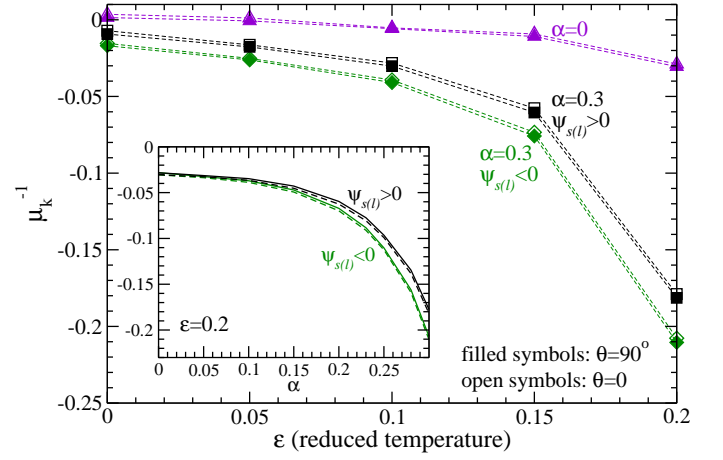


FIG. 10. (Color online) Inverse kinetic coefficient μ_k^{-1} as a function of reduced temperature ϵ , for $\alpha = 0$ and 0.3 . Inset: μ_k^{-1} vs solute expansion coefficient α at $\epsilon = 0.2$.

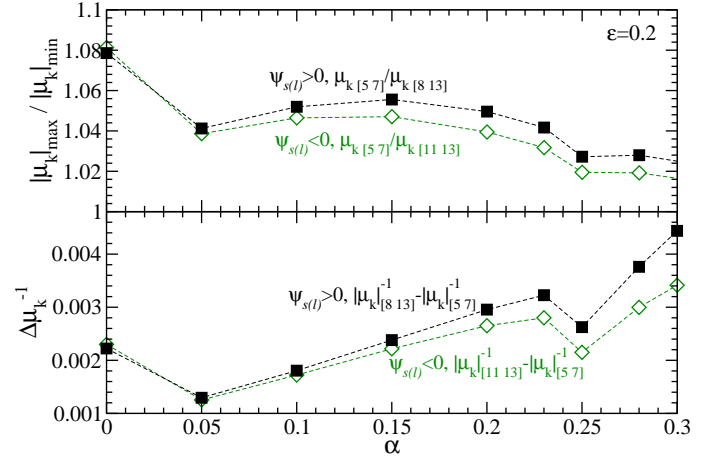


FIG. 11. (Color online) Anisotropy of kinetic coefficient as a function of solute expansion coefficient α at $\epsilon = 0.2$.

anisotropy (varying for different α values) is obtained at $\epsilon = 0.2$, with minimum (maximum) magnitude of μ_k found at orientation [8 13] with $\theta = 7.59^\circ$ ([5 7] with $\theta = 13.90^\circ$) for $\psi_{s(l)} > 0$, and at orientation [11 13] with $\theta = 21.79^\circ$ ([5 7] with $\theta = 13.90^\circ$) for $\psi_{s(l)} < 0$.

More interestingly, a scaling behavior can be identified for μ_k when plotted against the miscibility gap $\Delta\psi_0$. As shown in Fig. 12, data for various values of ϵ and α well converge to a universal curve $\mu_k^{-1} = a - b\Delta\psi_0^2$, although the scaling parameters a and b are different for positive and negative solidus/liquidus branches. Similar to the case discussed above, such a difference can be attributed to the effect of compositional strain. It causes the preferential segregation of larger (for $\psi_{s(l)} < 0$) or smaller (for $\psi_{s(l)} > 0$) atomic species on the solid surface and thus the compressive or tensile interface compositional stress, leading to different interface kinetics with smaller or larger values of μ_k respectively. This further demonstrates the important role played by the mesoscale cou-

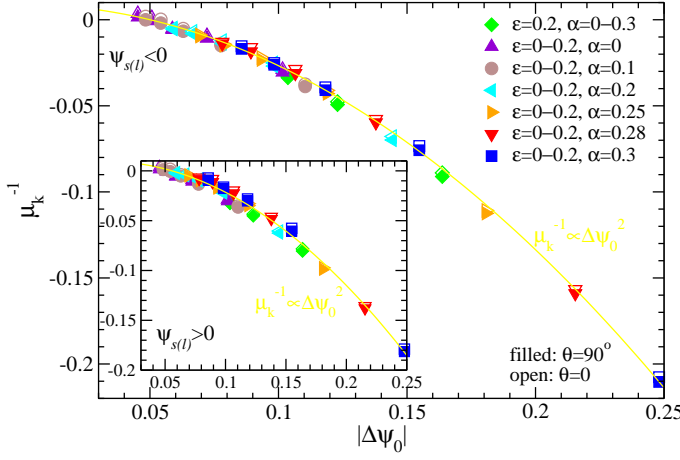


FIG. 12. (Color online) Scaling of μ_k^{-1} as a function of miscibility gap $\Delta\psi_0$, for different ranges of ϵ and α .

pling between the variation of alloy concentration field and the kinetics of interface structural profile.

Note that these results are for equal mobility of alloy constituents, i.e., $m = 0$. For nonzero mobility contrast values of μ_k should be multiplied by a factor of $1 - m^2$ (see Eq. (18)). This would then lead to $|\mu_k| \ll 1$ in the limit of $m \rightarrow \pm 1$ (with $M_A \gg M_B$ or $M_A \ll M_B$), consistent with the scenario of a frozen solid-liquid front due to the hindrance or pinning of one of the atomic components that is immobile.

C. Lattice pinning strength

There exists a fundamentally different type of pinning effect that originates from the micro-meso length scale coupling between microscopic lattice structure and mesoscopic interface amplitudes and concentration, as incorporated in Eqs. (16) and (19)–(26). This lattice coupling effect leads to two distinct modes of interface growth: As in the single-component case [35], the solid front will advance in a continuous mode when the magnitude of the thermodynamic driving force (i.e., $|\Delta|$) overcomes the lattice pinning strength p_0 ; otherwise when $|\Delta| < p_0$ the interface growth is characterized by a thermal activation and nucleation process, a scenario that is consistent with the crystal growth theory of Cahn [43]. For eutectic alloys our calculations show that p_0 is anisotropic as expected, as presented in Fig. 13 which gives the results of p_0 calculated from Eqs. (19)–(26) for two interface growth directions $\theta = 0$ (\hat{y} direction with strength p_{0y}) and $\theta = \pi/2$ (\hat{x} direction with strength p_{0x}). We obtain large crystalline anisotropy of p_0 , with ratio p_{0x}/p_{0y} ranging from 1.61 to 2.83 (see the inset of Fig. 13). Also for large enough compositional strain, this lattice pinning strength increases with the magnitude of α for both $\psi_{s(l)} > 0$ and < 0 and at both interface orientations.

Since this pinning effect is attributed to the nonadi-

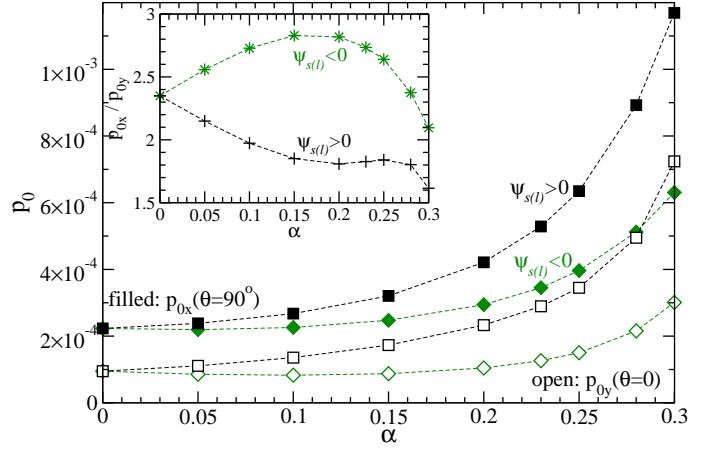


FIG. 13. (Color online) Pinning strength p_0 as a function of solute expansion coefficient α , for $\epsilon = 0.2$ and two different interface orientations $\theta = 0, \pi/2$. Inset: Anisotropy ratio of p_0 as a function of α .

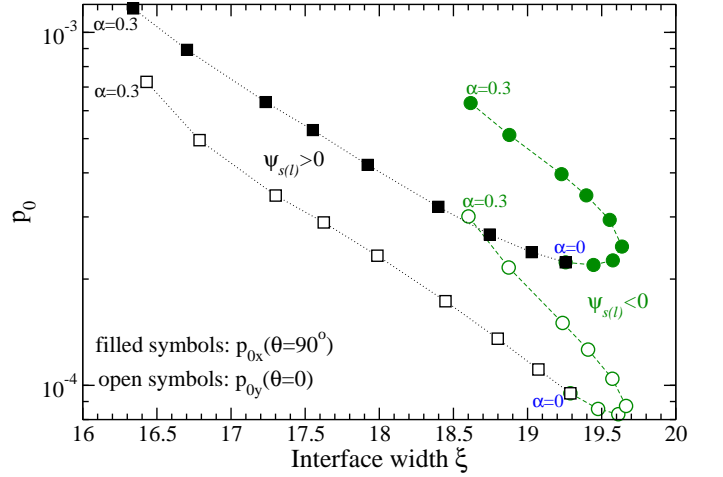


FIG. 14. (Color online) p_0 as a function of interface thickness ξ , for $\epsilon = 0.2$, $\alpha = 0 - 0.3$, $\psi_{s(l)} > 0$ (squares) and $\psi_{s(l)} < 0$ (circles).

abatic scale coupling at the interface, it is expected to increase with sharper interface and follow a universal relation $p_0 \sim \exp(-\alpha_p \xi)$ (with ξ the interface thickness and α_p a constant) for a given interface orientation as identified in pure systems [35]. However, for alloying systems this relation only holds within some limited ranges of ξ , while for wide enough interfaces a hysteresis-type behavior of p_0 vs ξ occurs, as shown in Fig. 14. This behavior arises from the coupling between structural and concentration profiles, causing another asymmetric effect of nonzero compositional strain. For liquid-solid interfaces of the same width ξ , larger (smaller) alloy components are enriched in the solid surface layer for $\psi_{s(l)} < 0$ (> 0) and $\alpha > 0$, leading to larger (smaller) pinning strength of the underlying interface lattice as illustrated in Fig. 14.

V. SUMMARY

We have systematically identified the effects of length-scale coupling and compositional stresses on key interfacial properties and their scaling behaviors for binary alloys, based on a complex PFC amplitude model and the corresponding coarse-graining scheme and sharp/thin-interface analysis. The method developed here can be directly applied to other 2D and 3D systems of different crystalline symmetries (as incorporated in the PFC models via modes selection and coupling). All of them can be reduced to effective 1D interfacial systems for different orientations as described above, making the calculation much more efficient as compared to previous atomistic computation efforts conducted in full dimensions. Importantly, this approach has incorporated system elasticity, crystalline symmetry and anisotropy, and couplings between different length scales that are missing in conventional continuum approaches.

It is also important to note that although what we study here is a model system, it can be parameterized to match to specific materials (via fitting to MD results of liquid-state direct correlation function and solid-state density amplitude [44, 45], to first-principles calculations [46], or to thermodynamics databases [47]). As such our method would provide a viable route for quantitatively determining key interfacial properties including interfacial free energy, kinetic coefficient, and lattice pinning that govern the material growth and solidification processes. Quantitative results of these interfacial properties should then depend on the atomistic specifics of the material examined. Nevertheless, the modeling scheme presented above is based on general principles of symmetry and length scale couplings (micro-meso and meso-meso). Thus some results obtained here, in particular the scaling behaviors identified, are expected to be intrinsic and not sensitive to microscopic details of alloy constituents and their interactions, a feature that is important for gaining fundamental insights of material properties.

ACKNOWLEDGMENTS

This work was supported by the National Science Foundation under Grant No. DMR-0845264.

Appendix A: Derivation of interface equations of motion with lattice pinning

We conduct a coarse-graining analysis of the nonadiabatic amplitude equations (4)–(8) and derive the corresponding anisotropic sharp/thin-interface equations of motion. Two derivation steps are needed: (i) The projection operator method [36] is used to obtain the interface equations in local curvilinear coordinates around a certain interface orientation. (ii) A variation method similar to that of Refs. [37, 38] is applied to the free energy of

the system, to identify the anisotropic form of the Gibbs-Thomson relation. Detailed results are given below, including the general formulation of interface equations and the corresponding interfacial quantities (in the case of varying n_0), as well as the simplified case of $n_0 = \text{const.}$ which leads to Eqs. (16)–(28) in Sec. III.

1. Interface equations for a fixed orientation $\theta = \theta_0$

Using the standard procedure of sharp/thin-interface approach [35, 36, 38], we first examine separately the inner region close to the interface and the outer region far from it via expanding the variables in orders of a small parameter ε (the interface Péclet number), and then match the inner and outer solutions to determine the interfacial boundary conditions. For a certain liquid-solid interface orientation θ_0 , we can assume $\theta(s) = \theta_0 + \varepsilon\tilde{\theta}$, where θ is the angle between the local normal direction \hat{n} of the interface and the \hat{y} axis. We also assume different scalings along and perpendicular to the interface normal in the inner region, i.e., u/ξ and $\varepsilon s/\xi$ (with ξ the interface thickness) for local curvilinear coordinates u and s . At $\mathcal{O}(1)$ we obtain the 1D equilibrium solutions $A'_j = A_j^0(u)$, $n_0 = n_0^0(u)$, and $\psi = \psi_0(u)$ for a planar interface oriented at θ_0 in the liquid-solid coexistence, i.e.,

$$\left. \frac{\delta \mathcal{F}}{\delta A_j^*} \right|_0 = 0, \quad \partial_u^2 \mu_\psi^0 = 0, \quad \partial_u^2 \mu_{n_0}^0 = 0, \quad (\text{A1})$$

where

$$\left. \frac{\delta \mathcal{F}}{\delta A_j^*} \right|_0 = \left. \frac{\partial f}{\partial A_j^*} \right|_0 + \mathcal{G}_j^0 (\mathcal{G}_j^0 - 2\delta_1^0) A_j^0 - 2q_0^2 \alpha [\psi_0 \mathcal{G}_j^0 A_j^0 + \mathcal{G}_j^0 (\psi_0 A_j^0)], \quad (\text{A2})$$

$$\begin{aligned} \mu_\psi^0 &= \left. \frac{\delta \mathcal{F}}{\delta \psi} \right|_0 = \mu_\psi^{\text{eq}} \\ &= \left. \frac{\partial f}{\partial \psi} \right|_0 - K_0 \partial_u^2 \psi_0 - 2q_0^2 \alpha \sum_j \left(A_j^{0*} \mathcal{G}_j^0 A_j^0 + \text{c.c.} \right) \end{aligned} \quad (\text{A3})$$

$$\mu_{n_0}^0 = \left. \frac{\partial f}{\partial n_0} \right|_0 = \mu_{n_0}^{\text{eq}}, \quad (\text{A4})$$

with

$$\begin{aligned} \mathcal{G}_{1,3}^0 &= \partial_u^2 + i(\mp 2q_x \sin \theta_0 - q_y \cos \theta_0) \partial_u, \\ \mathcal{G}_2^0 &= \partial_u^2 + 2iq_y \cos \theta_0 \partial_u. \end{aligned} \quad (\text{A5})$$

These 1D 0th-order solutions A_j^0 , n_0^0 , and ψ_0 are used in the calculations at $\mathcal{O}(\varepsilon)$, which lead to the following interface equations after matching the inner and outer expansions. The continuity conditions at the solid-liquid

interface are written as

$$v_n(\Delta n_0^0 - m\Delta\psi_0) = (1 - m^2) [\partial_u \delta\mu_{n_0}|_{0-} - \partial_u \delta\mu_{n_0}|_{0+}] \\ = (1 - m^2) [(\nabla \delta\mu_{n_0})_{\text{solid}} - (\nabla \delta\mu_{n_0})_{\text{liquid}}] \cdot \hat{\mathbf{n}}, \quad (\text{A6})$$

$$v_n(\Delta\psi_0 - m\Delta n_0^0) = (1 - m^2) [\partial_u \delta\mu_\psi|_{0-} - \partial_u \delta\mu_\psi|_{0+}] \\ = (1 - m^2) [(\nabla \delta\mu_\psi)_{\text{solid}} - (\nabla \delta\mu_\psi)_{\text{liquid}}] \cdot \hat{\mathbf{n}}, \quad (\text{A7})$$

where $\Delta n_0^0 = n_0^0(+\infty) - n_0^0(-\infty)$, $\Delta\psi_0 = \psi_0(+\infty) - \psi_0(-\infty)$, $\delta\mu_{n_0} = \mu_{n_0} - \mu_{n_0}^{\text{eq}}$, and $\delta\mu_\psi = \mu_\psi - \mu_\psi^{\text{eq}}$. The 1st-order outer equations governing the perturbations $\delta A_j = A'_j - A_j^0(\pm\infty)$, $\delta n_0 = n_0 - n_0^0(\pm\infty)$, and $\delta\psi = \psi - \psi_0(\pm\infty)$ are given by

$$\left. \frac{\partial f}{\partial A'_j} \right|_1 = 0, \quad (\text{A8})$$

$$\frac{\partial \delta n_0}{\partial t} = \nabla^2 \delta\mu_{n_0} + m \nabla^2 \delta\mu_\psi = \nabla^2 \left. \frac{\partial f}{\partial n_0} \right|_1 + m \nabla^2 \left. \frac{\partial f}{\partial \psi} \right|_1, \\ \frac{\partial \delta\psi}{\partial t} = m \nabla^2 \delta\mu_{n_0} + \nabla^2 \delta\mu_\psi = m \nabla^2 \left. \frac{\partial f}{\partial n_0} \right|_1 + \nabla^2 \left. \frac{\partial f}{\partial \psi} \right|_1.$$

At a moving interface the boundary condition is given by a generalized form of the Gibbs-Thomson relation that incorporates the coupling and pinning of the underlying lattice structure, i.e., for an interface orientation θ_0 ,

$$\mu_k^{-1} v_n = -\Delta - \gamma\kappa - p_0 \sin(qh_n + \varphi) + \eta_v, \quad (\text{A9})$$

where the thermodynamic driving force (interface supersaturation) $\Delta = q_0^2 [\Delta\psi_0 \delta\mu_\psi(0, s) + \Delta n_0^0 \delta\mu_{n_0}(0, s)]$, γ is the interfacial free energy expressed by Eq. (17) for a given $\theta = \theta_0$, and noise η_v is governed by

$$\langle \eta_v \rangle = 0, \quad \langle \eta_v(s, t) \eta_v(s', t') \rangle = 2D_v \delta(s - s') \delta(t - t'), \quad (\text{A10})$$

with $D_v = \vartheta q_0^2 \Gamma k_B T \mu_k^{-1}$. The kinetic coefficient μ_k is determined by

$$\mu_k^{-1} = (1 - m^2)^{-1} \int_{-\infty}^{+\infty} du \left\{ 2 \sum_j |\partial_u A_j^0|^2 \right. \\ \left. + q_0^2 [\psi_0^2 - \psi_0^2(\pm\infty) + n_0^{0^2} - n_0^{0^2}(\pm\infty) \right. \\ \left. - 2m (n_0^0 \psi_0 - n_0^0(\pm\infty) \psi_0(\pm\infty))] \right\}. \quad (\text{A11})$$

The lattice pinning strength p_0 and phase φ can be written in a general form

$$p_0 e^{i\varphi} = 2i [p_A(\theta_0) + p_\psi(\theta_0) + p_{n_0}(\theta_0)], \quad (\text{A12})$$

where p_ψ and p_A are given in Eqs. (20)–(26). Results of p_{n_0} are similar to those of p_ψ ; i.e., $p_{n_0} = 0$ for \mathbf{q}_j orientations ($\theta_0 = 0, \pm\pi/3$), and $p_{n_0} \neq 0$ for \mathbf{q}_{ij} orientations ($\theta_0 = \pi/2, \pm\pi/6$), with

$$p_{n_0} = q_0^2 \left\{ \left[\int_0^{+\infty} du n_0^0(u) \int_u^{+\infty} du' \right. \right. \\ \left. \left. - \int_{-\infty}^0 du n_0^0(u) \int_{-\infty}^u du' \right] I_0(u') \right. \\ \left. - \left(\int_0^{+\infty} du [n_0^0 - n_0^0(+\infty)] \right) \int_{-\infty}^{+\infty} du I_0(u) \right\}, \quad (\text{A13})$$

where $I_0(u) = \int_u^{u+a_x} du' e^{iqu'} f_{p_k}^*(u')/a_x$ with $k = 0, 1, 3$ for \mathbf{q}_{31} ($\theta_0 = \pi/2$), \mathbf{q}_{21} ($\theta_0 = \pi/6$), and \mathbf{q}_{23} ($\theta_0 = -\pi/6$) orientations.

2. Variation method and anisotropic formulation

For the case of varying local orientation θ , we can simply replace θ_0 by θ in the results given above, i.e., $\gamma(\theta_0) \rightarrow \gamma(\theta)$, $\mu_k(\theta_0, m) \rightarrow \mu_k(\theta, m)$, and $p_0(\theta_0) \rightarrow p_0(\theta)$. However, the corresponding anisotropic form of the Gibbs-Thomson relation is different, with additional terms associated with gradients of surface/interface tension [37]. Similar to the process of free energy variation used in Refs. [37, 38], for a system with non-moving ($v_n = 0$) interface we have

$$\delta(\mathcal{F} - \mathcal{F}_0) = 0, \quad (\text{A14})$$

given an infinitesimal perturbation of the interface with a perturbed hump around a reference point ($u = 0, s = s_0$). Here the system free energy $\mathcal{F} = \mathcal{F}_{\text{surface}} + \mathcal{F}_{\text{bulk}}$ with $\mathcal{F}_{\text{surface}} = \int ds \gamma(\theta)$ and $\mathcal{F}_{\text{bulk}} = -PV + \int d\mathbf{r} (\mu_\psi \psi + \mu_{n_0} n_0)$ for a system of pressure P and volume V , where $\mu_\psi, \psi, \mu_{n_0}, n_0$ are determined from solutions of Eq. (A8) in the outer region. \mathcal{F}_0 is the free energy of the equilibrium bulk state, i.e.,

$$\mathcal{F}_0 \simeq \int ds \left\{ \int_0^{+\infty} du [\mu_\psi^{\text{eq}} \psi_0(+\infty) + \mu_{n_0}^{\text{eq}} n_0^0(+\infty)] \right. \\ \left. + \int_{-\infty}^0 du [\mu_\psi^{\text{eq}} \psi_0(-\infty) + \mu_{n_0}^{\text{eq}} n_0^0(-\infty)] \right\} - PV,$$

where we have assumed $d\mathbf{r} = \int ds \int du (1 + u\kappa) \simeq \int ds \int du$ at the lowest order. Using the condition of Gibbs surface, we obtain

$$\mathcal{F} - \mathcal{F}_0 \simeq \int ds \gamma(\theta) + \int ds \int_{-\infty}^{+\infty} du (\delta\mu_\psi \psi + \delta\mu_{n_0} n_0). \quad (\text{A15})$$

It has been shown in Ref. [37] that

$$\delta \left(\int ds \gamma(\theta) \right) = (\gamma + d^2 \gamma / d\theta^2) \kappa \delta V \equiv (\gamma + \gamma'') \kappa \delta V, \quad (\text{A16})$$

where $\delta V = \int ds \delta u$. Also to first order of perturbations, the variation of 2nd term in Eq. (A15) yields

$$\delta \left[\int ds \int du (\delta\mu_\psi \psi + \delta\mu_{n_0} n_0) \right] \\ \simeq \int ds \int du \delta (\delta\mu_\psi \psi + \delta\mu_{n_0} n_0) \\ \simeq [\delta\mu_\psi(0, s_0) \Delta\psi_0 + \delta\mu_{n_0}(0, s_0) \Delta n_0^0] \delta V, \quad (\text{A17})$$

given $\delta\mu_\psi, \delta\mu_{n_0} \neq 0$ only around the interface $u = 0$ and $\delta(\delta\mu_\psi \psi + \delta\mu_{n_0} n_0) = [\partial_u (\delta\mu_\psi \psi + \delta\mu_{n_0} n_0)] \delta u + [\partial_s (\delta\mu_\psi \psi + \delta\mu_{n_0} n_0)] \delta s + \mathcal{O}(\delta u^2, \delta s^2)$. Thus the variation of free energy in Eq. (A14) becomes (for $q_0^2 = 1$ after rescaling)

$$-(\gamma + \gamma'') \kappa = \delta\mu_\psi(0, s_0) \Delta\psi_0 + \delta\mu_{n_0}(0, s_0) \Delta n_0^0 \equiv \Delta. \quad (\text{A18})$$

For the general case of moving interface with nonzero v_n and the lattice pinning effect given in Eq. (A9), the above relation can then be generalized to an anisotropic form of the Gibbs-Thomson condition

$$\mu_k^{-1}(\theta, m)v_n = -\Delta - [\gamma(\theta) + \gamma''(\theta)]\kappa - p_0(\theta)\sin(qh_n + \varphi(\theta)) + \eta_v, \quad (\text{A19})$$

which leads to Eq. (16).

3. Simplified case of $n_0 = \text{const.}$

Considering that for the liquid-solid interface of an alloy system the miscibility gap is mostly determined by the concentration field ψ and the variation of n_0 is much smaller, for simplicity we can approximate n_0 as a constant. Applying $\partial n_0 / \partial t = 0$ to Eq. (7) and combining it

with Eq. (8), we then reduce the dynamic equation of ψ to

$$\partial\psi/\partial t = (1 - m^2) \left\{ \nabla^2 \frac{\delta\mathcal{F}}{\delta\psi} - \int_x^{x \pm a_x} \frac{dx'}{a_x} \int_y^{y + a_y} \frac{dy'}{a_y} \left[f_{p_0'} e^{i\mathbf{q}_{13} \cdot \mathbf{r}'} + f_{p_1'} e^{i\mathbf{q}_{12} \cdot \mathbf{r}'} + f_{p_3'} e^{i\mathbf{q}_{32} \cdot \mathbf{r}'} + \text{c.c.} \right] \right\} + \nabla \cdot \boldsymbol{\eta}_{\psi_0},$$

where the noise term $\boldsymbol{\eta}_{\psi_0}$ is governed by

$$\langle \boldsymbol{\eta}_{\psi_0} \rangle = \langle \boldsymbol{\eta}_{\psi_0} \eta_j \rangle = \langle \boldsymbol{\eta}_{\psi_0} \eta_j^* \rangle = 0, \\ \langle \eta_{\psi_0}^\mu \eta_{\psi_0}^\nu \rangle = 2(1 - m^2) \vartheta_\psi \Gamma k_B T \delta(\mathbf{r} - \mathbf{r}') \delta(t - t') \delta^{\mu\nu}.$$

Following the same procedure of sharp/thin-interface analysis described above in Sec. A1 and Sec. A2, we can simplify the results of interface equations to those of Eqs. (16)–(28).

-
- [1] T. Haxhimali, A. Karma, F. Gonzales, and M. Rappaz, *Nat. Mater.* **5**, 660 (2006).
 - [2] M. Asta, C. Beckermann, A. Karma, W. Kurz, R. Napolitano, M. Plapp, G. Purdy, M. Rappaz, and R. Trivedi, *Acta Mater.* **57**, 941 (2009).
 - [3] S. Ghosh, A. Choudhury, M. Plapp, S. Bottin-Rousseau, G. Faivre, and S. Akamatsu, *Phys. Rev. E* **91**, 022407 (2015).
 - [4] J.-N. Aqua, I. Berbezier, L. Favre, T. Frisch, and A. Ronda, *Phys. Rep.* **522**, 59 (2013).
 - [5] D. Tsivion, M. Schwartzman, R. Popovitz-Biro, P. von Huth, and E. Joselevich, *Science* **333**, 1003 (2011).
 - [6] C. Tang and P. Harrowell, *Nat. Mater.* **12**, 507 (2013).
 - [7] L. Gránásy, T. Pusztai, T. Borzsonyi, J. A. Warren, and J. F. Douglas, *Nat. Mater.* **3**, 645 (2004).
 - [8] S. Liu, R. E. Napolitano, and R. Trivedi, *Acta Mater.* **49**, 4271 (2001); R. E. Napolitano and S. Liu, *Phys. Rev. B* **70**, 214103 (2004).
 - [9] C. Niederberger, J. Michler, and A. Jacot, *Phys. Rev. E* **74**, 021604 (2006).
 - [10] M. E. Glicksman and R. J. Schaefer, *J. Cryst. Growth* **1**, 297 (1967).
 - [11] G. H. Rodway and J. D. Hunt, *J. Cryst. Growth* **112**, 554 (1991).
 - [12] J. J. Hoyt, M. Asta, and A. Karma, *Phys. Rev. Lett.* **86**, 5530 (2001).
 - [13] C. A. Becker, D. Olmsted, M. Asta, J. J. Hoyt, and S. M. Foiles, *Phys. Rev. Lett.* **98**, 125701 (2007).
 - [14] M. Amini and B. B. Laird, *Phys. Rev. B* **78**, 144112 (2008).
 - [15] A. Kerrache, J. Horbach, and K. Binder, *Europhys. Lett.* **81**, 58001 (2008).
 - [16] S. R. Wilson and M. I. Mendelev, *Phil. Mag.* **95**, 224 (2015).
 - [17] A. A. Wheeler, W. J. Boettinger, and G. B. McFadden, *Phys. Rev. E* **47**, 1893 (1993).
 - [18] W. H. Shih, Z. Q. Wang, X. C. Zeng, and D. Stroud, *Phys. Rev. A* **35**, 2611 (1987).
 - [19] K.-A. Wu, C.-H. Wang, J. J. Hoyt, and A. Karma, *Phys. Rev. B* **91**, 014107 (2015).
 - [20] P. Harrowell and D. W. Oxtoby, *Phys. Rev. B* **33**, 6293 (1986).
 - [21] L. V. Mikheev and A. A. Chernov, *J. Cryst. Growth* **112**, 591 (1991).
 - [22] F. C. Larché and J. W. Cahn, *Acta Metall.* **33**, 331 (1985).
 - [23] J. E. Guyer and P. W. Voorhees, *Phys. Rev. Lett.* **74**, 4031 (1995).
 - [24] K. R. Elder, M. Katakowski, M. Haataja, and M. Grant, *Phys. Rev. Lett.* **88**, 245701 (2002); K. R. Elder, N. Provatas, J. Berry, P. Stefanovic, and M. Grant, *Phys. Rev. B* **75**, 064107 (2007).
 - [25] Z.-F. Huang and K. R. Elder, *Phys. Rev. Lett.* **101**, 158701 (2008); *Phys. Rev. B* **81**, 165421 (2010).
 - [26] H. Emmerich, H. Löwen, R. Wittkowski, T. Gruhn, G. I. Tóth, G. Tegze, and L. Gránásy, *Adv. Phys.* **61**, 665 (2012).
 - [27] K.-A. Wu, A. Adland, and A. Karma, *Phys. Rev. E* **81**, 061601 (2010).
 - [28] M. Greenwood, N. Provatas, and J. Rottler, *Phys. Rev. Lett.* **105**, 045702 (2010); M. Greenwood, N. Ofori-Opoku, J. Rottler, and N. Provatas, *Phys. Rev. B* **84**, 064104 (2011).
 - [29] S. K. Mkhonta, K. R. Elder, and Z.-F. Huang, *Phys. Rev. Lett.* **111**, 035501 (2013).
 - [30] M. Einax, W. Dieterich, and P. Maass, *Rev. Mod. Phys.* **85**, 921 (2013).
 - [31] A. M. van der Zande, P. Y. Huang, D. A. Chenet, T. C. Berkelbach, Y. You, G.-H. Lee, T. F. Heinz, D. R. Reichman, D. A. Muller, and J. C. Hone, *Nat. Mater.* **12**, 554 (2013).
 - [32] Z.-F. Huang, K. R. Elder, and N. Provatas, *Phys. Rev. E* **82**, 021605 (2010).
 - [33] N. Goldenfeld, B. P. Athreya, and J. A. Dantzig, *Phys. Rev. E* **72**, 020601(R) (2005); B. P. Athreya, N. Goldenfeld, and J. A. Dantzig, *Phys. Rev. E* **74**, 011601 (2006).
 - [34] K. R. Elder, Z.-F. Huang, and N. Provatas, *Phys. Rev. E* **81**, 011602 (2010).
 - [35] Z.-F. Huang, *Phys. Rev. E* **87**, 012401 (2013).

- [36] K. R. Elder, M. Grant, N. Provatas, and J. M. Kosterlitz, Phys. Rev. E **64**, 021604 (2001).
- [37] C. Herring, in *The Physics of Powder Metallurgy*, edited by W. E. Kingston (McGraw-Hill, New York, 1951) Chap. 8, pp. 143–179.
- [38] A. Karma and W.-J. Rappel, Phys. Rev. E **57**, 4323 (1998).
- [39] J. S. Langer, Rev. Mod. Phys. **52**, 1 (1980).
- [40] N. Eustathopoulos, Int. Met. Rev. **28**, 189 (1983).
- [41] F. Spaepen, Acta Metall. **23**, 729 (1975).
- [42] L. E. Murr, *Interfacial phenomena in metals and alloys* (Addison-Wesley, London, 1975).
- [43] J. W. Cahn, Acta Metall. **8**, 554 (1960); J. W. Cahn, W. B. Hillig, and G. W. Sears, **12**, 1421 (1964).
- [44] K.-A. Wu and A. Karma, Phys. Rev. B **76**, 184107 (2007).
- [45] A. Jaatinen, C. V. Achim, K. R. Elder, and T. AlaNissila, Phys. Rev. E **80**, 031602 (2009).
- [46] S. Muralidharan and M. Haataja, Phys. Rev. Lett. **105**, 126101 (2010).
- [47] N. Provatas and S. Majaniemi, Phys. Rev. E **82**, 041601 (2010).